Contents lists available at ScienceDirect

Surfaces and Interfaces

Tuning the morphology of sputter-deposited platinum catalyst: From compact layers to dispersed nanoparticles

Athira Lekshmi Mohandas Sandhya [a], Pavel Pleskunov [b], Marco Bogar [c], Xianxian Xie [a], Philipp Aldo Wieser [d], Martin Orság [a], Thu Ngan Dinhová [a], Milan Dopita [e], Rodolfo Taccani [c], Heinz Amenitsch [d], Andrei Choukourov [b], Iva Matolínová [a], Ivan Khalakhan [a],[*]

[a] *Department of Surface and Plasma Science, Faculty of Mathematics and Physics, Charles University, V Holešovičkách 2 Prague 8, 18000, Czech Republic*
[b] *Department of Macromolecular Physics, Faculty of Mathematics and Physics, Charles University, V Holešovičkách 2 Prague 8, 18000, Czech Republic*
[c] *Department of Engineering and Architecture, University of Trieste, Via Valerio 10, Trieste 34127, Italy*
[d] *Institute for Inorganic Chemistry, Graz University of Technology, Stremayrgasse 9, Graz 8010, Austria*
[e] *Department of Condensed Matter Physics, Faculty of Mathematics and Physics, Charles University, Ke Karlovu 5 Prague 2, 12116, Czech Republic*

ARTICLE INFO

ABSTRACT

A comprehensive study on adjusting the morphology of sputter-deposited platinum was performed. Platinum was deposited under various Ar pressure ranging from 0.3 to 3.2 Pa using a conventional magnetron system as well as at 57 Pa using a gas aggregation cluster source integrated into the magnetron sputtering system. The morphology and structure of deposited layers were characterized with a broad portfolio of characterization techniques such as scanning electron microscopy, transmission electron microscopy, grazing incidence small angle X-ray scattering and X-ray diffraction. The results revealed a continuous evolution of the Pt layer morphology from a thin-film-like layer of tightly packed Pt nanoparticles to a deposit composed of dispersed particles of 5-7 nm in size as the Ar pressure increased. The electrochemically active surface area of deposited Pt, as calculated from cyclic voltammograms, increased with deposition pressure from 11.7 $m^2 \cdot g_{Pt}^{-1}$ to 22.3 $m^2 \cdot g_{Pt}^{-1}$ and 24 $m^2 \cdot g_{Pt}^{-1}$ for Pt deposited at 0.3, 3.2 and 57 Pa, respectively. This increase in active sites was reflected in a significant improvement in the mass activity of platinum exemplary confirmed using a methanol electrooxidation reaction.

1. Introduction

Platinum remains the superior catalyst for a wide range of (electro) chemical reactions owing to its unique intrinsic properties. Particularly, Pt and Pt-based catalysts are vital for advanced clean energy conversion processes such as fuel cell technology, which is becoming increasingly important for the race towards cutting greenhouse gas emissions, as outlined in the recently announced Green Deal [1]. However, platinum is expensive and rare, and the expected increase in demand is likely to further increase its price [2]. Moreover, the catalytic activity of Pt degrades over time. The increase of platinum utilization and stability is thus of high importance.

Intensive research is currently underway to develop new or improved Pt or Pt-based catalysts with an improved activity-stability relationship. A significant step forward has been made addressing this aim in the last decade using several strategies, such as controlling the size and shape of Pt nanoparticle catalyst [3,4], incorporating specific elements into platinum to prepare Pt-based bimetallic [5–7] and even trimetallic alloys [8,9], etc. Despite significant progress, there is still ample opportunity for further catalyst improvement and innovation, especially with the rise of modern techniques which provide information about the catalyst directly in the course of the reaction of interest. Such techniques are expected to significantly contribute to obtaining fundamental knowledge that is a prerequisite for the development of novel catalysts for the next generation of fuel cell technologies.

Real fuel cell devices (full-cell), however, have a complex architecture comprising anode and cathode compartments, a solid polymer membrane, flow field desks, etc. Both the anode and cathode further consist of a catalyst deposited on a nanoporous layer, which in turn, is deposited on a microporous layer. Due to this complexity, characterizing the catalysts inside real fuel cells is relatively expensive and faces experimental difficulties. Instead, despite ongoing debates [10], the

---

majority of scientists focus their attention on the so-called liquid half-cells. The half-cell enables rapid and accurate catalyst inspection (either anode or cathode) under well-defined conditions. Studies in half-cell are well-suited for laboratory-scale studies due to their facile availability and low cost [11,12]. Furthermore, the half-cell configuration can be incorporated into specific characterization techniques, forming innovative experimental setups.

Electrodes for half-cell measurements are generally prepared on a planar surface of glassy carbon in a form of thin films composed of carbon-supported catalysts nanoparticles (NPs), mixed with an ionomeric polymer (so-called three-dimensional (3D) system). However, even such systems are rather complex because of possible support effects, mass transport limitations, contaminations from wet-chemical syntheses etc. Despite being far from real systems used in fuel cells, well-defined two-dimensional (2D) model electrodes of monolayer of evenly distributed NPs deposited on a planar substrate [6,13–17], or even single crystal electrodes [18–22], are being studied. These model electrodes are an inevitable part of the bottom-up approach in materials science and allow for elucidating fundamental aspects that are often undetectable in more complex systems. Furthermore, it broadens the portfolio of available techniques that can be combined with half-cells for those requiring flat planar substrates, including GISAXS, AFM, and STM [14,15,23–25].

Typically, nanoparticles for 2D electrodes are prepared using wet chemical synthesis and then precipitated onto the electrode surface, which can result in uneven nanoparticle distribution and aggregation. Moreover, they may contain surfactants used in synthesis that can be difficult to get rid of. As an alternative, magnetron sputtering deposition is a simple and fast method for scalable catalyst production of different compositions. More importantly, as a physical vapor deposition method, it allows the preparation of a catalyst free of toxic reactants and undesired surfactants, which underlines the undisputable advantage of this approach for catalyst preparation. Nevertheless, a sputter-deposited catalyst usually grows in a form of a compact layer rather than nanoparticles. On the other hand, sputtering deposition allows significant modification of the deposit morphology by simple variation of multiple deposition parameters such as background pressure, power on a magnetron, deposition angle, etc., opening a potential path for overcoming that limitation [26–32].

Herein, we report a comprehensive study on adjusting the morphology of sputter-deposited platinum by varying the sputtering deposition pressure, thereby aiming to get Pt deposited as one monolayer of nanoparticles assembly rather than compact layers to manufacture ultralow Pt loading electrodes for half-cell investigation. The comparative study is complemented by data from thorough characterization using multiple techniques and electrochemistry.

2. Experimental

2.1. Sample preparation

Multiple types of substrates were used to deposit Pt NP-based thin films: Si wafers (10 × 10 mm) covered by 10 nm of amorphous carbon layer to perform XRD and GISAXS measurements; carbon-coated copper grids (Agar Scientific) for HRTEM analysis and glassy carbon disks (Pine research, 5 mm diameter, 0.196 cm^2 surface area) substrates for cyclic voltammetry and SEM measurements.

2.1.1. Conventional magnetron sputtering system

Pt films were prepared by magnetron sputtering using a Circular TORUS magnetron (K. J. Lesker) with a 2-inch platinum target (99.99% Safina) placed under the angle of 45° and at the distance of 120 mm to the substrate. The deposition chamber was first evacuated to a base pressure of 4·10^{-4} Pa and then filled with Ar gas. Deposition under various Ar pressures was regulated by controlling the gas flow of argon. The Ar gas flow was set to 3.8, 18, 25, 39 and 49 sccm to have the

deposition chamber under the working gas pressures of 0.3, 0.8, 1.9, 2.6 and 3.2 Pa respectively. The deposition was carried out at a constant sputtering power of 60 W. A series of depositions were performed controlling deposition time in order to deposit Pt films with as much as possible equal thickness of approximately 7 nm.

A rough estimation of the Pt loading in each sample was provided as follows. Mass loading was calculated by multiplying the Pt density by the total Pt area and Pt thickness. A compact layer with the thickness of 7 nm (obtained from GISAXS measurements) would have 15 $\mu g_{Pt}\cdot cm^{-2}$. To estimate the Pt loading in all samples, a thresholding tool was applied to SEM images to determine the relative area occupied by particles and voids. The Pt loading of each sample was then estimated to be lower than 15 $\mu g_{Pt}\cdot cm^{-2}$ by the percentage of voids present in corresponding SEM images.

2.1.2. Gas aggregation cluster source integrated into magnetron sputtering system

A custom-built gas aggregation cluster source (GAS) equipped with a 3-inch planar magnetron was used to extend the working conditions to the higher pressures. The GAS source was mounted vertically onto the main vacuum chamber. The system was evacuated to a base pressure of 1·10^{-5} Pa by turbomolecular and scroll pumps. Then, Ar was injected into the GAS via a mass flow controller with the flow rate set to 18 sccm to form the working pressure of 57 Pa. The magnetron was powered by dc power supply operated in constant current mode. The Pt target (99.99% Safina) underwent pre-cleaning for 5 minutes with a magnetron current of 350 mA, then the current was reduced to 250 mA. A more detailed description of the GAS can be found elsewhere [33–35]. The distance between the exiting orifice of the GAS source and the substrates was 100 mm.

The mass of deposited Pt was assessed via the mass flux of Pt NPs. The NP mass flux is defined as the total mass of material that is deposited onto a substrate unit area for a given period of time. The Pt NP mass flux, j_m was calculated by finding the volume of every NP observed within the SEM micrograph view field, summing all the volumes and calculating the deposited mass onto the unit area per time with an assumption that the density of bulk Pt at standard temperature and pressure (STP) is approximately equal to 21.45 g·cm^{-3}. To simplify the calculations, single Pt NP volume was approximated by a volume of model cubic NP with the side length equal to the NP size measured by HRTEM.

$$j_m = \frac{\rho \sum l^3}{A_{SEM} t}$$

Here, ρ is the density of the Pt at STP, l is the NP side length, A_{SEM} is the area of the SEM view field, t is the deposition time.

2.2. Physical characterization

The morphology was studied by means of Scanning Electron Microscope (SEM) using a Tescan Mira 3 microscope operated at 30 keV beam energy and Transmission Electron Microscopy (TEM) using a JOEL-2200FS microscope operated at 200 keV. For TEM characterization platinum layers were deposited directly on copper grids covered with a holey carbon film (Agar scientific). The SEM images taken on Pt thin films sputtered at low pressures were analyzed using ImageJ software, while the Matlab Image Processing Toolkit (IPT) was applied for the processing of SEM images acquired on Pt$_{GAS}$ NPs. Both software packages allow for expeditious and robust analysis of coatings with complex topology.

Grazing Incidence Small Angle X-Ray Scattering (GISAXS) patterns were recorded *ex situ* at room temperature and pressure at the Austrian SAXS beamline at the ELETTRA synchrotron in Trieste, Italy [36] by means of a 2D Pilatus3 1M detector (Dectris), at a beam energy of 16 keV, and with a sample-to-detector distance equal to 200.58 cm. Silver behenate was used as a calibrant of the q-scale and the incidence angle was set to 0.3° above the sample surface. IGOR Pro 7.0.8.1

(Wavemetrics) was used for data reduction and analysis. Two cuts retrieved with the Nika package for IGOR Pro [37] were used for further data analysis: the in-plane cut, retrieved by integrating the two-dimensional scattering patterns at the height of the Yoneda wings, while the out-of-plane cut was obtained by integrating the scattering patterns along the vertical direction, at the horizontal position of the specular peak. The in-plane cut was then processed by least-square fitting by means of an analytical model developed within previous studies [14,23,24], where deposited Pt nanoparticles were modelled by means of the product of a form factor, P(q), and a structure factor, S(q): $I(q) \propto P(q, I_P, \overline{D_P}, \sigma_P) \cdot S(q, R_{SHS}, \varphi, \lambda, \varepsilon)$. As the form factor P(q), a set of spheres which sizes follow the Schulz distribution [38] was selected. Here, the particle size distribution is described in terms of the mean particle size ($\overline{D_P}$) and standard deviation (σ_P), while I_P represents the forwarded scattering probability of the particles population. The so-called Sticky-Hard-Sphere model was then used as the structure factor S(q) [39]. Here, from R_{SHS} the minimum interparticle distance can be calculated, the apparent volume fraction (φ), which is related to the probability to find a nearest neighbor particle, and λ and ε, representing the width and the depth of the potential well, respectively. In order to calculate the average distance between the centers of nearest neighbor particles (d_{NN}), the first correlation peak of the structure factor was fitted with a Gaussian probability distribution function. Then the average nearest neighbor distance was retrieved by the so-obtained peak position (q*) as $d_{NN} = 2\pi/q^*$. Finally, from the out-of-plane cut, the analysis focused on the periodicity of the Kiessig fringes [40]: two consecutive peaks of the fringes were singularly fit by using a model composed by the sum of a Gaussian probability distribution function (modelling the peak of the fringe) and a power law (modelling the background). From the fringe periodicity (Δq), obtained by the difference of displacement of two consecutive peaks, the estimated sample thickness was calculated as: $t = 2\pi/\Delta q$ [41,42].

X-ray diffraction (XRD) measurements were performed using a SmartLab diffractometer (Rigaku) equipped with a 9 kW rotating anode X-ray source (Cu Kα radiation, $\lambda = 0.15418$ nm), a parabolic multilayer mirror in the primary beam, a set of axial divergence eliminating Soller slits with acceptance 5° in both incident and diffracted beam, and a HighPix-3000 2D hybrid pixel single-photon counting detector. The XRD measurements were done in the parallel beam-glancing angle X-ray diffraction geometry (GAXRD) with a parallel beam Soller slit collimator (acceptance 0.5°) in the diffracted beam. The constant angle of the incidence beam of 0.6° was used for the measurements.

2.3. Electrochemical characterization

The voltammograms were recorded in an N_2 purged 0.1M $HClO_4$ and 0.1M $HClO_4$ + 0.5M CH_3OH solutions at 200 mV·s^{-1} and 50 mV·s^{-1} sweep rates, respectively, in a typical 3 electrode half-cell (Pine research) configuration, where the platinum deposited onto glassy carbon (Pine research, 5 mm diameter, 0.196 cm^2 surface area) acted as a working electrode, platinum wire as a counter electrode (Pine research) and Ag/AgCl in saturated KCl as a reference electrode (Monokrystaly s.r. o.). The system was connected to SP-150 potentiostat (Bio-Logic). All electrochemical measurements were performed at room temperature. All the potentials here are referring to a reversible hydrogen electrode (RHE). EC-Lab (Bio-Logic) software was used for the data processing. The electrochemically active surface area (ECSA) was calculated by integrating the double-layer corrected area of the CV curve in the hydrogen underpotential deposition (H_{UPD}) region and dividing it by a value of 210 μC·cm^{-2} corresponding to a monolayer of adsorbed hydrogen atoms on platinum.

3. Results and discussions

The series of SEM and HRTEM images of approximately 7 nm thick Pt

sputtered layers on a planar glassy carbon substrate at different deposition pressures along with Pt sputtered in GAS configuration at an Ar pressure of 57 Pa (hereafter denoted as Pt_{GAS}) are shown in the upper and middle rows of Fig. 1, respectively. As can be visible in the SEM image, the Pt deposited at the lowest Ar pressure of 0.3 Pa forms a compact layer. The corresponding HRTEM image shows that the film is comprised of tightly packed randomly oriented crystallites with a lateral dimension of about 5 nm. With increasing Ar pressure, the deposit becomes less compact, with the appearance of voids and their further expansion demonstrating clear transformation to rougher and more porous layer [43]. At 3.2 Pa the deposit morphology approaches that of one monolayer of homogeneously distributed nanoparticles with a lateral diameter of approximately 5 nm as highlighted in the corresponding HRTEM image. Finally, the Pt_{GAS} sample exhibits a monolayer of evenly distributed nanoparticles of different shapes. The nanoparticles are slightly larger with a wider size distribution (5-10 nm) compared to Pt deposited at 3.2 Pa.

In support of electron microscopy observations, GISAXS patterns were collected, as represented in the bottom row of Fig. 1, and better highlighted in the horizontal and vertical cuts shown in Figs 2a and 2b, respectively. With increasing Ar pressure the Pt layer transforms from a thin-film-like layer made of tightly packed Pt nanoparticles towards a layer composed of more dispersed particles. Such evolution reflects in both fading out of the fringes developing along the out-of-plane direction, as well as remarkable differences in the low-q region of the horizontal cut, due to the shift towards lower q values of the first correlation peak of the structure factor, related to the increased distance among Pt nanoparticles, as well evidenced in SEM images.

Fig. 2 summarizes the results of fitting the in-plane and out-of-plane cuts made from measured patterns with an analytical model developed and validated in our previous studies [14,23,24]. The evolution of the main parameters composing the analytical model was found to be consistent with the electron microscopy images presented above. The particle size distribution in Fig. 2c shows a relatively narrow distribution for Pt deposited using the conventional magnetron sputtering system. The mean particle size was found to slightly decrease with increasing pressure, from about 6 nm for 0.3 Pa to about 4 nm for 3.2 Pa. On the other hand, Pt deposited using the GAS system revealed larger particles with a significantly wider size distribution. The average nearest neighbor distance (distance between particles center) in Fig. 2d showed a steep increase with increasing Ar pressure, accompanied by a decreasing trend in the apparent volume fraction (Fig. 2e) indicating decrease of the packing density of the particles. This behavior points to the formation of more dispersed Pt nanoparticles for higher values of gas pressure which is consistent with SEM and TEM results.

The analysis of the Kiessig fringes from the out-of-plane cuts (Fig. 2f) allowed the determination of the thickness of the deposited Pt layers. It is noteworthy that in the case of the Pt_{GAS} sample, no fringes were detected (see green curve in Fig. 2b) and it was not possible to extract any information from the out-of-plane cut. Nevertheless, in this case, the mean particle size can be considered being equal to the layer thickness (as highlighted by the triangle mark in Fig. 2f) since a monolayer of particles was deposited. The thickness was found to be almost constant at about 7 ± 1 nm for all investigated samples. Therefore, we can exclude the influence of the layer thickness on the morphological evolution presented above, which indeed is solely related to the background Ar pressure.

It is also worth mentioning that SEM images and the asymmetry in the GISAXS patterns point to the fact that deposition seems directional at lower pressures which is attributed to the geometry of the conventional sputtering device (Pt target is placed at a 45° angle with respect to the sample). Such preferential orientation at lower sputtering pressure is given by the fact that initial nuclei tend to grow in the direction of available coating flux, similar to what was observed earlier [35]. This directionality, however, begins to fade out as the sputtering pressure increases which can be attributed to an increase in collisions between
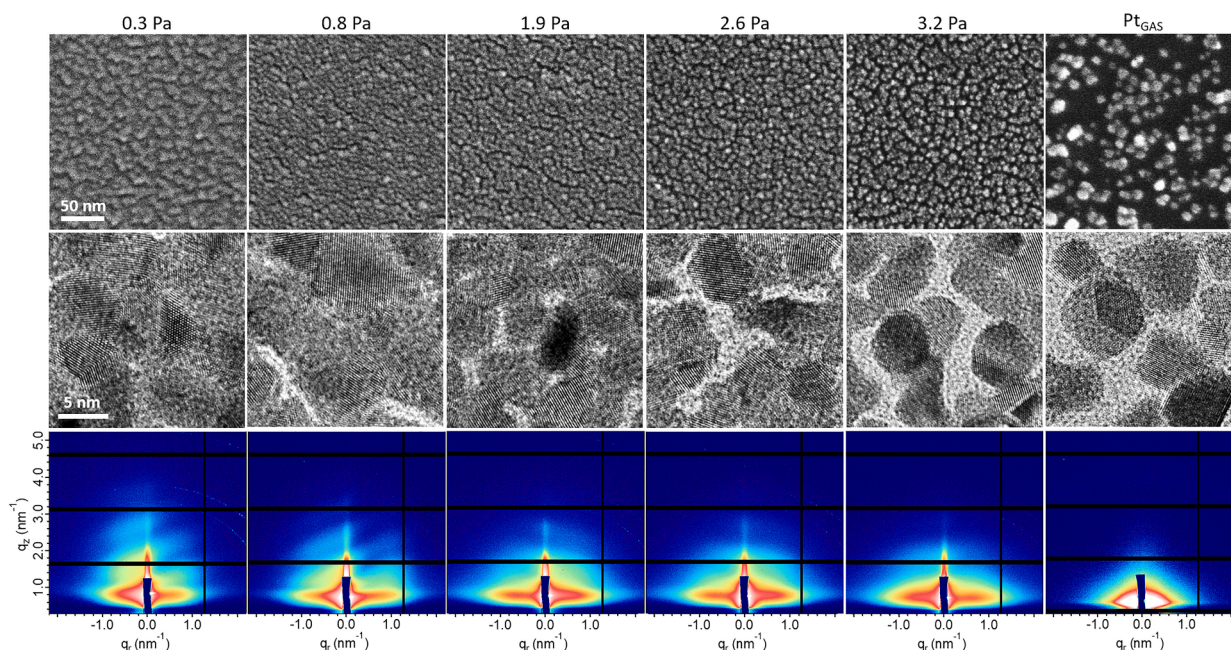
Fig. 1. SEM (upper row), TEM (middle row) images and GISAXS scattering patterns (bottom row) of platinum sputtered at varying deposition pressure.

the Pt particles and the background gas atoms which leads to a more isotropic film structure.

The impact of Ar pressure on the film structure is well established and attributed to the modifications in the kinetic energy of sputtered Pt atoms. When the argon Ar pressure is low, the collision mean free path of sputtered Pt atoms is greater, which increases the probability that hyperthermal atoms reach the substrate, bearing sufficient energy to overcome the surface diffusion barriers, rearrange themselves by hopping, and form a more compact film [28,44–46]. As a result, the films prepared at lower pressures (i.e. < 1 Pa) reach the percolation threshold and are continuous in nature with a minor fraction of voids as can be seen from HRTEM micrographs. At higher pressures, (i.e. > 1 Pa) the sputtered atoms suffer frequent collisions with Ar atoms before arriving to the substrate surface, and their energy distribution is shifted to lower energies. This essentially restricts the mobility of newly arrived atoms, resulting in roughening of the film topology. Additionally, limited surface diffusion leads to the development of uneven underlying layer topology. This results in a self-shadowing effect advancing the island growth even further. Thus, discontinuous films below the percolation threshold are produced. This is confirmed by greater fraction of voids observed on HRTEM micrographs taken on the films sputtered at higher Ar pressures. Finally, the NP films produced at 57 Pa are far below the percolation threshold and exhibit a localized (i.e. between two or more neighboring NPs) continuity given the stochastic nature of the inter-particle distance variation.

The structure of the magnetron sputtered Pt layers was further determined by means of XRD. The acquired XRD diffractograms in Fig. 3 reveal a typical polycrystalline nature of platinum deposits, with a single phase of the face-centered cubic (FCC) (space group Fm-3m, no. 225) structure regardless of the sputtering Ar pressure. The crystallite size and lattice constant were determined from the corresponding diffractograms. Yet, we did not observe any clear dependence of the mean crystallite size and lattice constant on deposition pressure. The crystallite size of all samples deposited using conventional magnetron sputtering varies around approximately 5 nm. while the one for Pt$_{GAS}$ was calculated to be about 8 nm which agrees well with microscopy and GISAXS studies above. The lattice constant for all samples was estimated to be 3.9230 ± 0.0015 Å corresponding to that of platinum.

Cyclic voltammetry was then employed to determine the influence of the sputtering pressure and resulting morphological changes on the active surface area of the platinum catalyst. Fig. 4a represents the set of CV curves acquired for platinum deposited at different working gas pressures. All CVs reveal a typical shape for polycrystalline Pt in a perchloric acid solution showing sharp hydrogen and oxygen redox features separated by a double-layer region. Even though the shape of CV curves persists as the deposition pressure increases, a recognizable difference is observed in the area under the main peaks evidencing changes in the Pt surface exposed to the electrolyte i.e., Pt active surface area.

The ECSA was quantified from the corresponding CV curves using the charge of the hydrogen desorption region, emerging within 0.05-0.35 V_{RHE} on the anodic scan of CVs shown in Fig. 4a. The calculated Pt loadings (details can be found in the experimental part) were 15, 14.5, 13.7, 13.1, 11.5 and 5.6 $\mu g_{Pt} \cdot cm^{-2}$ for 0.3, 0.8, 1.9, 2.6, 3.2 and 57 Pa, respectively. The ECSA as a function of the Ar pressure together with selected SEM images illustrating morphological changes is depicted in Fig. 4b. At the beginning it shows a linear increase with deposition pressure, evidencing nearly double increase of the ECSA at 3.2 Pa (22.3 $m^2 \cdot g_{Pt}^{-1}$) with respect to 0.3 Pa (11.7 $m^2 \cdot g_{Pt}^{-1}$) indicating significant increase of accessible active sites as Pt layer transforms from compact layer to separated nanoparticles. The ECSA increases even further with sputtering pressure but rather saturates reaching only 24 $m^2 \cdot g_{Pt}^{-1}$ for Pt deposited at 57 Pa using the GAS sputtering setup.

A further question arises of how the above-described catalyst surface modifications induced by sputtering pressure affect its reactivity. This we demonstrate by evaluating catalyst activity toward methanol electrooxidation reaction (MOR) in the alkaline electrolyte as an exemplary reaction. Fig. 4c displays CVs acquired in 0.1M HClO$_4$ + 0.5M CH$_3$OH solution for Pt deposited at the lowest (0.3 Pa) and the highest (3.2 Pa) studied pressures in the conventional magnetron setup with the one deposited at 57 Pa in the GAS. The cyclic voltammogram of MeOH electrooxidation for all samples exhibits two peaks. The more intense oxidation peak (J_f) at about 0.85 V_{RHE} in the forward scan is related to initial methanol electrooxidation, while another less intense oxidation peak (J_b) at about 0.65 V_{RHE}) in the backward scan is attributed to the oxidation of carbon-containing intermediate products formed during methanol electrooxidation in the forward scan. The Pt$_{GAS}$ sample exhibited the highest current density, implying higher activity towards MOR with increasing sputtering pressure. These results are consistent with ECSA in Fig. 4b. The charge of the methanol oxidation peaks, i.e.
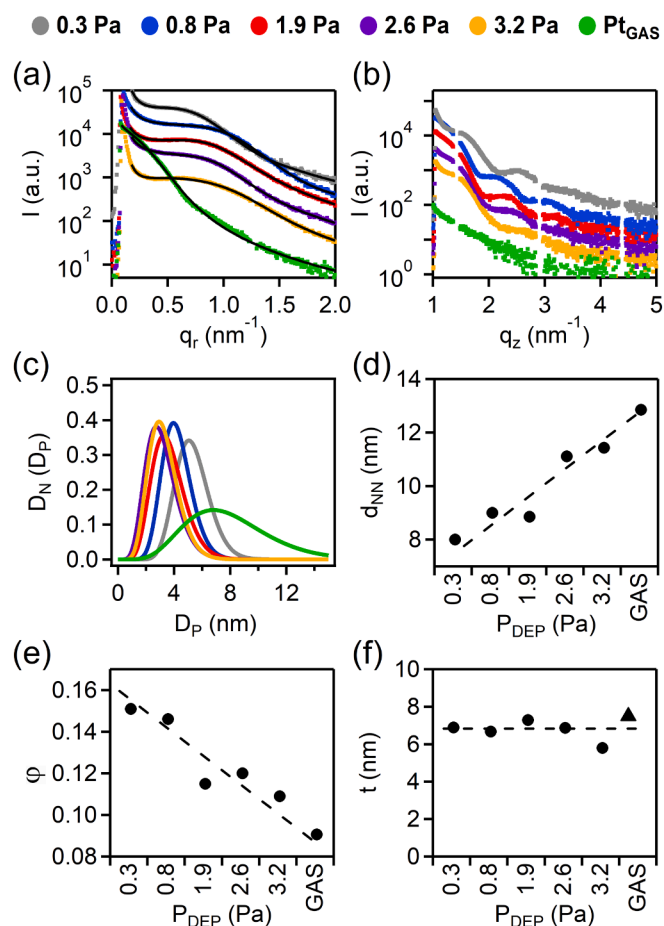
Fig. 2. GISAXS characterization. (a) in-plane and (b) out-of-plane cuts obtained from measured scattering patterns. For the in-plane cuts, the curve representing the fit with the analytical model is drawn in black on top of the 1D patterns. (c, d, and e) Main parameters retrieved from fitting the in-plane cuts with the analytical model: particle size distribution, $D_N(D_P)$, average nearest neighbor distance (d_{NN}) and the apparent volume fraction (φ), which is related to the probability of finding a nearest neighbor particle. (f) Calculated Pt layer thickness (t) from analyzing the Kiessig fringes of the out-of-plane cut.
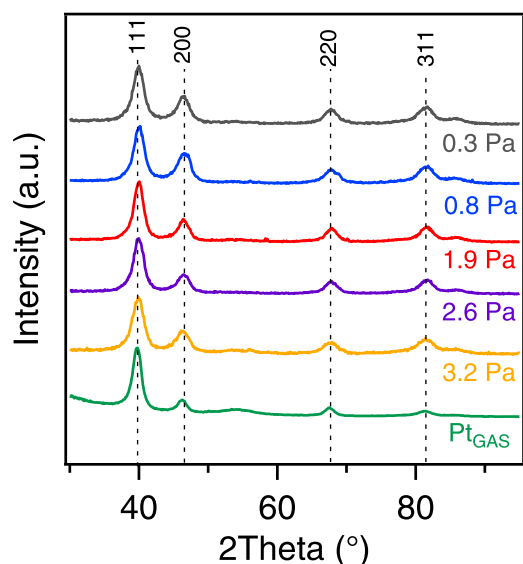

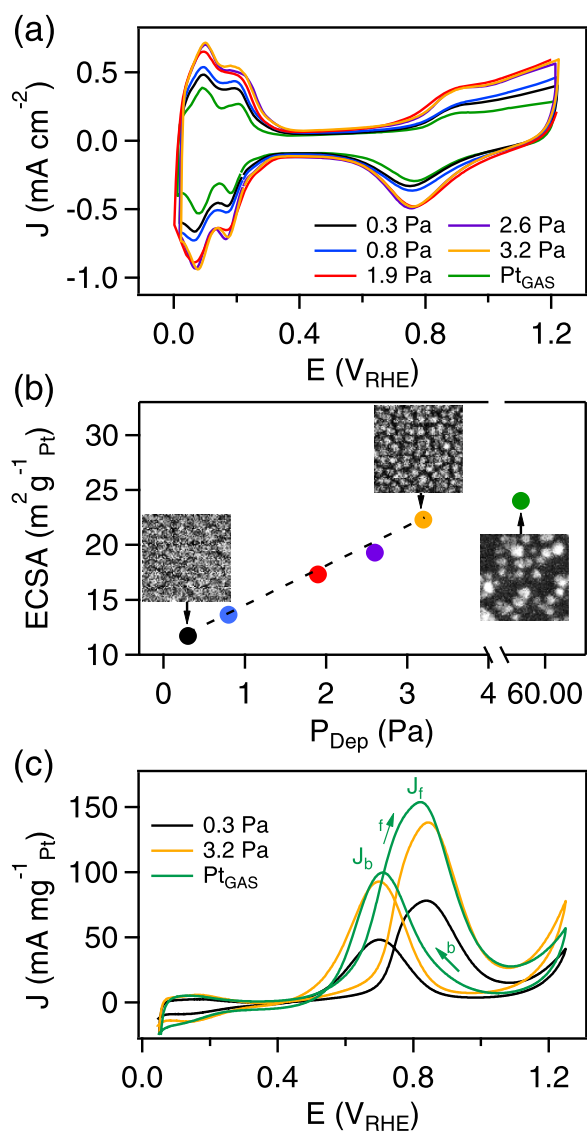**Fig. 3.** XRD patterns of platinum sputtered at varying deposition pressure.

Fig. 4. (a) Cyclic voltammograms for Pt deposited in 0.3, 0.8, 1.9, 2.6 and 3.2 Pa of Ar pressure in conventional magnetron system and Pt deposited using GAS system recorded in N_2-saturated 0.1M $HClO_4$ at 200 mV·s^{-1} sweep rate; (b) evolution of ECSA calculated from cycling voltammograms shown in (a) together with selected SEM images for Pt deposited at 0.3, 3.2 and 57 Pa; (c) Cyclic voltammograms for Pt deposited in 0.3, 3.2 Pa of Ar pressure in conventional magnetron system and Pt deposited using GAS system recorded in N_2-saturated 0.1M $HClO_4$ + 0.5M CH_3OH solution at 50 mV·s^{-1} sweep rate.

the catalyst activity, increased by 77 % for the sample deposited under 3.2 Pa of Ar pressure as compared to 0.3 Pa. For the Pt_{GAS} sample, the activity further increases by 12 %. On the other hand, the shape of CV curves, the peak position and the J_f/J_b ratio more or less persist with an increase in the deposition pressure implying identical reaction mechanisms (Table 1).

The above results prove the effectiveness of the sputtering pressure

Table. 1
Catalytic performance of platinum sputtered at different deposition pressure for methanol electrooxidation in 0.1M $HClO_4$ + 0.5M CH_3OH solution at 50 mV·s^{-1} sweep rate.

	J_f (mA·mg$_{Pt}^{-1}$)	J_b (mA·mg$_{Pt}^{-1}$)	J_f/J_b
0.3 Pa	78	48	1.60
3.2 Pa	138	93	1.50
Pt_{GAS}	154	100	1.55

for precise engineering of magnetron sputtered platinum layers as well-defined 2D model electrodes composed of a monolayer of evenly distributed NPs deposited on a planar substrate. Since a large number of material combinations at different compositions are accessible for the sputtering technology this method can be applied to other material systems. This opens up new possibilities for tailoring the properties of sputtered materials for diverse applications across various fields.

4. Conclusions

We reported a systematic study on adjusting the morphology of sputter-deposited platinum catalyst from a compact thin-film layer to a monolayer of dispersed nanoparticles by varying the deposition pressure. The comparative study was supported by thorough characterization using multiple techniques and electrochemistry.

Background Ar pressure ranging from 0.3 to 3.2 Pa was utilized in the conventional magnetron system while 57 Pa in the gas aggregation cluster source integrated into the magnetron sputtering system. With increasing pressure, the morphology of Pt deposit gradually transformed from a compact layer to a monolayer of separated nanoparticles. This resulted in a significant increase of ECSA from $11.7\ \mathrm{m^2 \cdot g_{Pt}^{-1}}$ for compact Pt layer to $24\ \mathrm{m^2 \cdot g_{Pt}^{-1}}$ for Pt nanoparticles. The abundance of active sites manifested in a significant improvement in the mass activity of platinum, as confirmed by a methanol electrooxidation reaction.

The simplicity of magnetron sputter deposition together with easy control of Pt deposit morphology underlines the indisputable advantage of this approach for the fast and scalable preparation of free from toxic reactants and undesired surfactants low-loading electrodes for model half-cell investigation.

CRediT authorship contribution statement

Athira Lekshmi Mohandas Sandhya: Investigation, Data curation, Writing – original draft, Writing – review & editing. **Pavel Pleskunov:** Investigation, Formal analysis, Writing – original draft, Writing – review & editing. **Marco Bogar:** Investigation, Data curation, Writing – original draft, Writing – review & editing. **Xianxian Xie:** Investigation, Formal analysis. **Philipp Aldo Wieser:** Investigation, Formal analysis. **Martin Orság:** Investigation, Formal analysis. **Thu Ngan Dinhová:** Investigation, Formal analysis. **Milan Dopita:** Investigation, Formal analysis. **Rodolfo Taccani:** Writing – review & editing. **Heinz Amenitsch:** Data curation, Writing – review & editing. **Andrei Choukourov:** Supervision, Data curation, Writing – original draft. **Iva Matolínová:** Supervision, Data curation, Writing – original draft. **Ivan Khalakhan:** Supervision, Data curation, Funding acquisition, Conceptualization, Project administration, Writing – original draft, Writing – review & editing.

Declaration of Competing Interest

The authors declare that they have no known competing financial interests or personal relationships that could have appeared to influence the work reported in this paper.

Data availability

Data will be made available on request.

Acknowledgments

References

[1] The European Commission, A European Green Deal. https://ec.europa.eu/info/strategy/priorities-2019-2024/european-green-deal_en.

[2] G. Reverdiau, A.Le Duigou, T. Alleau, T. Aribart, C. Dugast, T. Priem, Will there be enough platinum for a large deployment of fuel cell electric vehicles? Int. J. Hydrogen Energy 46 (2021) 39195–39207.

[3] M. Li, Z. Zhao, T. Cheng, A. Fortunelli, C.-Y. Chen, R. Yu, Q. Zhang, L. Gu, B. V Merinov, Z. Lin, E. Zhu, T. Yu, Q. Jia, J. Guo, L. Zhang, W.A. Goddard, Y. Huang, X. Duan, Ultrafine jagged platinum nanowires enable ultrahigh mass activity for the oxygen reduction reaction, Science 354 (2016) 1414–1419.

[4] B. Garlyyev, K. Kratzl, M. Rück, J. Michalička, J. Fichtner, J.M. Macak, T. Kratky, S. Günther, M. Cokoja, A.S. Bandarenka, A. Gagliardi, R.A. Fischer, Optimizing the size of platinum nanoparticles for enhanced mass activity in the electrochemical oxygen reduction reaction, Angew. Chemie Int. Ed. 58 (2019) 9596–9600.

[5] C. Chen, Y. Kang, Z. Huo, Z. Zhu, W. Huang, H.L. Xin, J.D. Snyder, D. Li, J. A. Herron, M. Mavrikakis, M. Chi, K.L. More, Y. Li, N.M. Markovic, G.A. Somorjai, P. Yang, V.R. Stamenkovic, Highly crystalline multimetallic nanoframes with three-dimensional electrocatalytic surfaces, Science 343 (2014) 1339–1343.

[6] P. Hernandez-Fernandez, F. Masini, D.N. McCarthy, C.E. Strebel, D. Friebel, D. Deiana, P. Malacrida, A. Nierhoff, A. Bodin, A.M. Wise, J.H. Nielsen, T. W. Hansen, A. Nilsson, I.E.L. Stephens, I. Chorkendorff, Mass-selected nanoparticles of Pt$_x$Y as model catalysts for oxygen electroreduction, Nat. Chem. 6 (2014) 732–738.

[7] J. Li, S. Sharma, X. Liu, Y.T. Pan, J.S. Spendelow, M. Chi, Y. Jia, P. Zhang, D. A. Cullen, Z. Xi, H. Lin, Z. Yin, B. Shen, M. Muzzio, C. Yu, Y.S. Kim, A.A. Peterson, K.L. More, H. Zhu, S. Sun, Hard-magnet L1$_0$-CoPt nanoparticles advance fuel cell catalysis, Joule 3 (2019) 124–135.

[8] J. Zhu, M. Xie, Z. Chen, Z. Lyu, M. Chi, W. Jin, Y. Xia, Pt-Ir-Pd Trimetallic nanocages as a dual catalyst for efficient oxygen reduction and evolution reactions in acidic media, Adv. Energy Mater. 10 (2020), 1904114.

[9] L. Bu, J. Ding, S. Guo, X. Zhang, D. Su, X. Zhu, J. Yao, J. Guo, G. Lu, X. Huang, A general method for multimetallic platinum alloy nanowires as highly active and stable oxygen reduction catalysts, Adv. Mater. 27 (2015) 7204–7212.

[10] C.Y. Ahn, J.E. Park, S. Kim, O.-H. Kim, W. Hwang, M. Her, S.Y. Kang, S. Park, O. J. Kwon, H.S. Park, Y.H. Cho, Y.E. Sung, Differences in the electrochemical performance of Pt-based catalysts used for polymer electrolyte membrane fuel cells in liquid half- and full-cells, Chem. Rev. 121 (2021) 15075–15140.

[11] Y. Garsany, O.A. Baturina, K.E. Swider-Lyons, S.S. Kocha, Experimental methods for quantifying the activity of platinum electrocatalysts for the oxygen reduction reaction, Anal. Chem. 82 (2010) 6321–6328.

[12] M. Povia, J. Herranz, T. Binninger, M. Nachtegaal, A. Diaz, J. Kohlbrecher, D. Abbott, B. Kim, T.J. Schmidt, Combining SAXS and XAS to study the operando degradation of carbon-supported Pt-nanoparticle fuel cell catalysts, ACS Catal. 8 (2018) 7000–7015.

[13] D.J.S. Sandbeck, N.M. Secher, F.D. Speck, J.E. Sørensen, J. Kibsgaard, I. Chorkendorff, S. Cherevko, Particle size effect on platinum dissolution: Considerations for accelerated stability testing of fuel cell catalysts, ACS Catal. 10 (2020) 6281–6290.

[14] M. Bogar, Y. Yakovlev, D.J.S. Sandbeck, S. Cherevko, I. Matolínová, H. Amenitsch, I. Khalakhan, Interplay among dealloying, Ostwald Ripening, and coalescence in Pt$_x$Ni$_{100-x}$ bimetallic alloys under fuel-cell-related conditions, ACS Catal. 11 (2021) 11360–11370.

[15] I. Khalakhan, A. Choukourov, M. Vorokhta, P. Kús, I. Matolínová, V. Matolín, In situ electrochemical AFM monitoring of the potential-dependent deterioration of platinum catalyst during potentiodynamic cycling, Ultramicroscopy 187 (2018) 64–70.

[16] M. Ahmadi, F. Behafarid, C. Cui, P. Strasser, B.R. Cuenya, Long-range segregation phenomena in shape-selected bimetallic nanoparticles: Chemical state effects, ACS Nano 7 (2013) 9195–9204.

[17] X. Xie, V. Briega-Martos, R. Farris, M. Dopita, M. Vorokhta, T. Skála, I. Matolínová, K.M. Neyman, S. Cherevko, I. Khalakhan, Optimal Pt–Au alloying for efficient and stable oxygen reduction reaction catalysts, ACS Appl. Mater. Interfaces. 15 (2023) 1192–1200.

[18] L. Jacobse, Y.F. Huang, M.T.M. Koper, M.J. Rost, Correlation of surface site formation to nanoisland growth in the electrochemical roughening of Pt, Nat. Mater. 17 (111) (2018) 277–282.

[19] P.P. Lopes, D. Li, H. Lv, C. Wang, D. Tripkovic, Y. Zhu, R. Schimmenti, H. Daimon, Y. Kang, J. Snyder, N. Becknell, K.L. More, D. Strmcnik, N.M. Markovic, M. Mavrikakis, V.R. Stamenkovic, Eliminating dissolution of platinum-based electrocatalysts at the atomic scale, Nat. Mater. 19 (2020) 1207–1214.

[20] J. Drnec, M. Ruge, F. Reikowski, B. Rahn, F. Carlà, R. Felici, J. Stettner, O. M. Magnussen, D.A. Harrington, Initial stages of Pt(111) electrooxidation: dynamic and structural studies by surface X-ray diffraction, Electrochim. Acta. 224 (2017) 220–227.

[21] T. Fuchs, J. Drnec, F. Calle-Vallejo, N. Stubb, D.J.S. Sandbeck, M. Ruge, S. Cherevko, D.A. Harrington, O.M. Magnussen, Structure dependency of the atomic-scale mechanisms of platinum electro-oxidation and dissolution, Nat. Catal. 3 (2020) 754–761.

[22] M. Ruge, J. Drnec, B. Rahn, F. Reikowski, D.A. Harrington, F. Carlà, R. Felici, J. Stettner, O.M. Magnussen, Structural reorganization of Pt(111) electrodes by electrochemical oxidation and reduction, J. Am. Chem. Soc. 139 (2017) 4532–4539.

[23] M. Bogar, I. Khalakhan, A. Gambitta, Y. Yakovlev, H. Amenitsch, In situ electrochemical grazing incidence small angle X-ray scattering: From the design of

an electrochemical cell to an exemplary study of fuel cell catalyst degradation, J. Power Sources. 477 (2020), 229030.

[24] I. Khalakhan, M. Bogar, M. Vorokhta, P. Kúš, Y. Yakovlev, M. Dopita, D.J. S. Sandbeck, S. Cherevko, I. Matolínová, H. Amenitsch, Evolution of the PtNi bimetallic alloy fuel cell catalyst under simulated operational conditions, ACS Appl. Mater. Interfaces. 12 (2020) 17602–17610.

[25] I. Khalakhan, M. Vorokhta, M. Václavů, B. Šmíd, J. Lavková, I. Matolínová, R. Fiala, N. Tsud, T. Skála, V. Matolín, In-situ electrochemical atomic force microscopy study of aging of magnetron sputtered Pt–Co nanoalloy thin films during accelerated degradation test, Electrochim. Acta. 211 (2016) 52–58.

[26] O.K. Alexeeva, V.N. Fateev, Application of the magnetron sputtering for nanostructured electrocatalysts synthesis, Int. J. Hydrogen Energy. 41 (2016) 3373–3386.

[27] K. Fu, L. Zeng, J. Liu, M. Liu, S. Li, W. Guo, Y. Gao, M. Pan, Magnetron sputtering a high-performance catalyst for ultra-low-Pt loading PEMFCs, J. Alloys Compd. 815 (2020), 152374.

[28] E. Slavcheva, G. Ganske, G. Topalov, W. Mokwa, U. Schnakenberg, Effect of sputtering parameters on surface morphology and catalytic efficiency of thin platinum films, Appl. Surf. Sci. 255 (2009) 6479–6486.

[29] A. Bonakdarpour, M.D. Fleischauer, M.J. Brett, J.R. Dahn, Columnar support structures for oxygen reduction electrocatalysts prepared by glancing angle deposition, Appl. Catal. A Gen. 349 (2008) 110–115.

[30] K. Makino, K. Furukawa, K. Okajima, M. Sudoh, Optimization of the sputter-deposited platinum cathode for a direct methanol fuel cell, Electrochim. Acta. 51 (2005) 961–965.

[31] F. Wang, H. Zhao, J. Liang, T. Li, Y. Luo, S. Lu, X. Shi, B. Zheng, J. Du, X. Sun, Magnetron sputtering enabled synthesis of nanostructured materials for electrochemical energy storage, J. Mater. Chem. A. 8 (2020) 20260–20285.

[32] M.D. Gasda, R. Teki, T.M. Lu, N. Koratkar, G.A. Eisman, D. Gall, Sputter-deposited Pt PEM fuel cell electrodes: Particles vs layers, J. Electrochem. Soc. 156 (2009) B614.

[33] O. Kylián, V. Valeš, O. Polonskyi, J. Pešička, J. Čechvala, P. Solař, A. Choukourov, D. Slavínská, H. Biederman, Deposition of Pt nanoclusters by means of gas aggregation cluster source, Mater. Lett. 79 (2012) 229–231.

[34] P. Pleskunov, T. Košutová, M. Vaidulych, D. Nikitin, Z. Krtouš, S. Ali-Ogly, K. Kishenina, R. Tafiichuk, H. Biederman, I. Gordeev, J. Drewes, I. Barg, F. Faupel,

M. Cieslar, R. Yatskiv, Y. Pihosh, V. Nandal, K. Seki, K. Domen, A. Choukourov, The sputter-based synthesis of tantalum oxynitride nanoparticles with architecture and bandgap controlled by design, Appl. Surf. Sci. 559 (2021), 149974.

[35] K. Biliak, D. Nikitin, S. Ali-Ogly, M. Protsak, P. Pleskunov, M. Tosca, A. Sergievskaya, D. Cornil, J. Cornil, S. Konstantinidis, T. Košutová, Z. Černochová, P. Štěpánek, J. Hanuš, J. Kousal, L. Hanyková, I. Krakovský, A. Choukourov, Plasmonic Ag/Cu/PEG nanofluids prepared when solids meet liquids in the gas phase, Nanoscale Adv. 5 (2023) 955–969.

[36] H. Amenitsch, M. Rappolt, M. Kriechbaum, H. Mio, P. Laggner, S. Bernstorff, First performance assessment of the small-angle X-ray scattering beamline at ELETTRA, J. Synchrotron Radiat. 5 (1998) 506–508.

[37] J. Ilavsky, Nika: software for two-dimensional data reduction, J. Appl. Crystallogr. 45 (2012) 324–328.

[38] M. Kotlarchyk, S.H. Chen, Analysis of small angle neutron scattering spectra from polydisperse interacting colloids, J. Chem. Phys. 79 (1983) 2461–2469.

[39] R.V Sharma, K.C. Sharma, The structure factor and the transport properties of dense fluids having molecules with square well potential, a possible generalization, Phys. A Stat. Mech. Its Appl. 89 (1977) 213–218.

[40] H. Kiessig, Untersuchungen zur Totalreflexion von Röntgenstrahlen, Ann. Phys. 402 (1931) 715–768.

[41] A. Gibaud, S. Hazra, X-ray reflectivity and diffuse scattering, Curr. Sci. 78 (2000) 1467–1477.

[42] U. Pietsch, V. Holy, T. Baumbach, High-Resolution X-Ray Scattering : From Thin Films to Lateral Nanostructures, Springer-Verlag New York Inc., 2004.

[43] J.H. Thomas, Effect of pressure on dc planar magnetron sputtering of platinum, J. Vac. Sci. Technol. A. 21 (2003) 572–576.

[44] P. Andreazza, C. Andreazza-Vignolle, J.P. Rozenbaum, A.L. Thomann, P. Brault, Nucleation and initial growth of platinum islands by plasma sputter deposition, Surf. Coatings Technol. (2002) 122–127, 151–152.

[45] K. Khojier, H. Savaloni, S. Zolghadr, On the dependence of structural and sensing properties of sputtered MoO_3 thin films on argon gas flow, Appl. Surf. Sci. 320 (2014) 315–321.

[46] E. Slavcheva, G. Topalov, G. Ganske, I. Radev, E. Lefterova, U. Schnakenberg, Influence of sputtering pressure on surface structure and oxygen reduction reaction catalytic activity of thin platinum films, Electrochim. Acta. 55 (2010) 8992–8997.